

Mathematical Models and Methods in Applied Sciences  
© World Scientific Publishing Company

## **ALE–VMS Formulation for Stratified Turbulent Incompressible Flows with Applications**

Y. BAZILEVS, A. KORO BENKO, J. YAN

*Structural Engineering, University of California, San Diego  
9500 Gilman Drive, La Jolla, CA 92093, USA*

A. PAL, S.M.I. GOHARI, S. SARKAR

*Mechanical and Aerospace Engineering, University of California, San Diego  
9500 Gilman Drive, La Jolla, CA 92093, USA*

Received (Day Month Year)

Revised (Day Month Year)

Communicated by (xxxxxxxxxx)

A numerical formulation for incompressible flows with stable stratification is developed using the framework of variational multiscale methods. In the proposed formulation, both density and temperature stratification are handled in a unified manner. The formulation is augmented with weakly-enforced essential boundary conditions and is suitable for applications involving moving domains, such as fluid–structure interaction. The methodology is tested using three numerical examples ranging from flow-physics benchmarks to a simulation of a full-scale offshore wind-turbine rotor spinning inside an atmospheric boundary layer. Good agreement is achieved with experimental and computational results reported by other researchers. The wind-turbine rotor simulation showed that flow stratification has a strong influence on the dynamic rotor thrust and torque loads.

*Keywords:* ALE–VMS; Stratified flow; Turbulence; Internal gravity waves; Self-propelled wake; Atmospheric boundary layer; Wind turbine

AMS Subject Classification: 22E46, 53C35, 57S20

### **1. Introduction**

Flows with density and temperature stratification (here referred to as stratified flows) play an important role in many geophysics applications. Examples of stratified flows include oceanic and atmospheric flows over topography, mixing in the upper ocean layers, and wakes behind towed or self-propelled objects. In many cases these are high-Reynolds-number turbulent flows, where turbulent motions are strongly affected by the presence of stratification.

In the case of wake flows, the presence of the buoyancy force strongly affects turbulent mixing and decay rates. In a decaying wake velocity fluctuations in the direction of gravity become small in comparison with the remaining components, which hampers the wake growth in this direction and leads to a so-called wake collapse. The flow reorganizes into a quasi-2D state, with the appearance of large-scale “pancake”-like vortices [1,2]. To date,

2 *Y. Bazilevs, A. Korobenko, J. Yan, A. Pal, S.M.I. Gohari, and S. Sarkar*

most of the numerical simulations of turbulent wakes with density stratification using large-eddy simulation (LES) and direct numerical simulation (DNS) techniques are based on temporal wake evolution. Only a few researchers recently performed spatially-evolving wake simulations (see, e.g., [3, 4]), which are more challenging due to high computational costs associated with the need to use long computational domains and resolve small-scale turbulent fluctuations [5].

Stably-stratified atmospheric boundary layers (ABLs) present another set of challenges for modeling and simulation (see, e.g., [6]). Besides exhibiting more complex interaction of turbulent structures with the mean flow than are present in classical turbulent boundary layers, these flows often possess a host of complex, but non-turbulent structures, including wave-like motions, solitary modes, and two-dimensional vortical modes. The inversion layer, where the wind shear is strong, is an additional source of turbulence whose interaction with the near-surface turbulence is known to be important but is poorly understood. Finally, the turbulence is typically not in equilibrium with the non-turbulent motions, which often prevents formation of the inertial subrange. The latter presents significant challenges for turbulence modeling, especially for classical eddy-viscosity-based LES models that rely on the presence of the inertial subrange [7].

Accurate simulation of stably-stratified ABLs is important for realistic modeling of wind-turbine aerodynamics and fluid-structure interaction (FSI) at full scale, especially for making predictions about power production, rotor loading, and blade structural response. Attempts were made in the direction of LES simulation of ABL interacting with the wind-turbine structure represented using an actuator disk model [8–10]. In the present work we simulate a 5 MW wind-turbine rotor in an ABL, where the rotor is represented with full geometric complexity. To our knowledge this is the first time such a computation is reported in open literature. The computation is enabled through a collaboration between two groups with expertise in FSI and environmental turbulence, respectively.

In this paper, motivated by the above challenges, we develop a numerical formulation for stratified incompressible flows. The ALE-VMS method, proposed in this work for the simulation of stratified flows, originated from the residual-based variational multiscale (RBVMS) formulation of incompressible turbulent flows proposed in [11] for stationary domains, and may be thought of as an extension of the RBVMS method to moving domains handled using the Arbitrary Lagrangian-Eulerian (ALE) [12] technique. ALE-VMS was presented for the first time in [13] in the context of FSI. ALE-VMS gave very good results for several important turbulent flows. However, it was evident in [11, 14] that in order to obtain accurate results for wall-bounded turbulent flows the method required relatively fine resolution of boundary layers, making ALE-VMS a somewhat costly computational technology. For this reason, weakly-enforced essential boundary condition formulation was introduced in [15], which significantly improved the performance of the ALE-VMS formulation in the presence of under-resolved boundary layers [16–18]. In the present paper, weak boundary conditions are formulated and applied in the context of stratified flows. The ALE-VMS technique was successfully applied to several challenging problems, including full-scale 3D aerodynamics and FSI of horizontal- and vertical-axis wind turbines [19–26], FSI of compliant hydrofoils [27], patient-specific cardiovascular FSI [28, 29], and FSI of

bioprosthetic heart valves [30, 31].

Recently, an RBVMS formulation was derived in [32, 33] in the context of space-time (ST) finite element methods in fluid mechanics [34–38], which is called ST-VMS in [22, 26, 28, 29, 39, 40]. ST-VMS was successfully applied to wind-turbine aerodynamics [19, 41–44], flapping-wing aerodynamics [44–51], cardiovascular fluid mechanics [44, 50, 52–55], spacecraft aerodynamics [56], and thermo-fluid analysis of ground vehicles and their tires [57]. The original version of the stabilized ST method, which is now called ST-SUPS (see [33] for the terminology), has also been successfully used in addressing the challenges involved in FSI problems [58], including cardiovascular FSI (see [39]) and spacecraft parachute FSI (see [39] for earlier examples, and [59–64] for newer examples).

The paper outline is as follows. In Section 2 we present the governing equations and develop the semi-discrete ALE–VMS formulation of incompressible stratified flows. In Section 3 we present three numerical examples employing our numerical methodology. The first example is a 2D test case where we show that our framework is able to reproduce internal gravity waves that are consistent with the theoretical and experimental findings. We then simulate the evolution of a self-propelled wake at  $Re = 15,000$  and provide comparison with the recent DNS simulation results of this test case [4]. We conclude the section by presenting a simulation of a full-scale 5 MW offshore wind-turbine rotor in an ABL with temperature stratification. In Section 4 we draw conclusions and discuss future work.

## 2. ALE–VMS Formulation of Stratified Flows

### 2.1. Governing equations of stratified flows on moving domains

To model stratified flow we use Navier–Stokes equations of incompressible flows with the Boussinesq approximation. The Navier–Stokes equations with the Boussinesq approximation are posed on a moving spatial domain, and are written in the ALE frame [12] as follows:

$$\rho \left( \frac{\partial \mathbf{u}}{\partial t} \Big|_{\hat{\mathbf{x}}} + (\mathbf{u} - \hat{\mathbf{u}}) \cdot \nabla \mathbf{u} - \mathbf{f} \right) - \nabla \cdot \boldsymbol{\sigma} - \mathbf{b} = \mathbf{0} \quad \text{in } \Omega, \quad (2.1)$$

$$\nabla \cdot \mathbf{u} = 0 \quad \text{in } \Omega. \quad (2.2)$$

Here  $\Omega$  is the problem domain,  $\mathbf{f}$  is the external force per unit mass,  $\mathbf{u}$  and  $\hat{\mathbf{u}}$  are velocities of the fluid and problem domain, respectively. The stress tensor  $\boldsymbol{\sigma}$  is defined as

$$\boldsymbol{\sigma}(\mathbf{u}, p) = -p\mathbf{I} + 2\mu\boldsymbol{\varepsilon}(\mathbf{u}), \quad (2.3)$$

where  $p$  is the pressure,  $\mathbf{I}$  is the identity tensor,  $\mu$  is the dynamic viscosity, and  $\boldsymbol{\varepsilon}(\mathbf{u})$  is the strain-rate tensor given by

$$\boldsymbol{\varepsilon}(\mathbf{u}) = \frac{1}{2} (\nabla \mathbf{u} + \nabla \mathbf{u}^T). \quad (2.4)$$

In Eq. (2.1),  $\Big|_{\hat{\mathbf{x}}}$  denotes the time derivative taken with respect to a fixed referential domain spatial coordinates  $\hat{\mathbf{x}}$ . The spatial derivatives in the above equations are taken with respect to the spatial coordinates  $\mathbf{x}$  of the current configuration.

4 *Y. Bazilevs, A. Korobenko, J. Yan, A. Pal, S.M.I. Gohari, and S. Sarkar*

A time-dependent scalar advection-diffusion equation, also posed on a moving spatial domain in the ALE frame, is added to the model and is written as

$$\left. \frac{\partial \phi}{\partial t} \right|_{\hat{x}} + (\mathbf{u} - \hat{\mathbf{u}}) \cdot \nabla \phi - \nabla \cdot \kappa \nabla \phi - f = 0 \quad \text{in } \Omega. \quad (2.5)$$

The Navier–Stokes and advection-diffusion equations exhibit two-way coupling: The scalar field  $\phi$  enters the Navier–Stokes momentum equation through the Boussinesq term denoted by  $\mathbf{b}$  in Eq. (2.1), while the fluid velocity  $\mathbf{u}$  appears in the convective term in Eq. (2.5).

Depending on the physical phenomena modeled, Eq. (2.5) describes the evolution of the fluid density or temperature field. The two cases are distinguished in what follows.

*Density stratification.* Here  $\phi$  is associated with with the non-dimensional fluid density, and is defined as follows:

$$\phi(\mathbf{x}, t) = \rho_0 + \bar{\rho}(x_3) + \rho'(\mathbf{x}, t). \quad (2.6)$$

Here the fluid density  $\rho(\mathbf{x}, t)$  is decomposed into a constant background field denoted by  $\rho_0$ , a linearly varying field in the  $x_3$ -direction denoted by  $\bar{\rho}(x_3)$ , and a fluctuating field with full space and time dependence denoted by  $\rho'(\mathbf{x}, t)$ . The Boussinesq forcing term may be written as  $\mathbf{b} = B\hat{\mathbf{b}}$ , where  $B$  is the characteristic dimension and  $\hat{\mathbf{b}}$  takes on the form

$$\hat{\mathbf{b}} = -\frac{\rho'}{Fr^2} \mathbf{e}_3. \quad (2.7)$$

Here,  $\mathbf{e}_3$  is the Cartesian basis vector,  $Fr$  is the Froude number, a non-dimensional parameter defined as

$$Fr = \frac{U}{ND}, \quad (2.8)$$

where  $U$  and  $D$  are the characteristic velocity and length scales. In Eq. (2.8),  $N$  is the so-called Brunt–Vaisala frequency [65, 66] defined as

$$N^2 = -\frac{g}{\rho_0} \frac{\partial \bar{\rho}}{\partial x_3}, \quad (2.9)$$

where  $g$  is the gravitational acceleration magnitude. Note that the definition given by Eq. (2.9) is meaningful in the case of negative vertical density gradient (i.e., lighter fluid on top and heavier fluid on the bottom), which is what defines stable stratification.

*Temperature stratification.* This form is typically employed in atmospheric boundary layer (ABL) modeling. Here  $\phi$  is associated with with the fluid potential temperature, and is defined as follows:

$$\phi(\mathbf{x}, t) = \bar{\theta}(x_3) + \theta'(\mathbf{x}, t). \quad (2.10)$$

Here the fluid temperature  $\theta(\mathbf{x}, t)$  is decomposed into the background field varying in the  $x_3$ -direction denoted by  $\bar{\theta}(x_3)$ , and a fluctuating field with full space and time dependence denoted by  $\theta'(\mathbf{x}, t)$ . The Boussinesq term  $\mathbf{b}$  takes on the form

$$\mathbf{b} = \rho g \frac{\theta'}{\theta_0} \mathbf{e}_3, \quad (2.11)$$

where  $\theta_0$  is the reference temperature assumed constant in the Boussinesq approximation.

In the case of ABL the Earth rotation effects may be important. For this the Coriolis force is applied in the momentum equation Eq. (2.1) as

$$\mathbf{f} = f_c \epsilon_{ijk} u_j \mathbf{e}_i, \quad (2.12)$$

where  $f_c$  is the Coriolis parameter and  $\epsilon_{ijk}$ 's are the Cartesian components of the alternator tensor.

## 2.2. Semi-discrete formulation of stratified flow

The weak form of the stratified-flow equations in the ALE framework is stated as follows: Find  $\mathbf{u}$ ,  $p$ , and  $\phi$ , the fluid velocity, pressure, and scalar fields, respectively, such that for all  $\mathbf{w}$ ,  $q$ , and  $\eta$ , the linear-momentum-, incompressibility-, and advection-diffusion-equation test functions, respectively:

$$\begin{aligned} & \int_{\Omega} \mathbf{w} \cdot \rho \left( \frac{\partial \mathbf{u}}{\partial t} \Big|_{\hat{x}} + (\mathbf{u} - \hat{\mathbf{u}}) \cdot \nabla \mathbf{u} - \mathbf{f} \right) d\Omega + \int_{\Omega} \boldsymbol{\varepsilon}(\mathbf{w}) : 2\mu \boldsymbol{\varepsilon}(\mathbf{u}) d\Omega - \int_{\Gamma_h} \mathbf{w} \cdot \mathbf{h} d\Gamma - \int_{\Omega} \mathbf{w} \cdot \mathbf{b} \\ & + \int_{\Omega} q \nabla \cdot \mathbf{u} d\Omega + \int_{\Omega} \eta \left( \frac{\partial \phi}{\partial t} \Big|_{\hat{x}} + (\mathbf{u} - \hat{\mathbf{u}}) \cdot \nabla \phi - f \right) + \int_{\Omega} \nabla \eta \cdot \kappa \nabla \phi d\Omega - \int_{\Gamma_h^\phi} \eta h d\Gamma = 0, \end{aligned} \quad (2.13)$$

where  $\Gamma_h$  and  $\Gamma_h^\phi$  are the subsets of the domain boundary with traction and flux boundary conditions prescribed for the Navier–Stokes and advection–diffusion equations, respectively, and  $\mathbf{h}$  and  $h$  are the prescribed traction and flux values.

We use the RBVMS technique [11, 39, 67, 68] in the ALE frame (i.e., the ALE–VMS technique) to discretize the equations in space. ALE–VMS relies on the decomposition of the solution and test-function fields into coarse and fine scales as

$$\begin{aligned} \mathbf{u} &= \mathbf{u}^h + \mathbf{u}', \\ p &= p^h + p', \\ \phi &= \phi^h + \phi', \\ \mathbf{w} &= \mathbf{w}^h + \mathbf{w}', \\ q &= q^h + q', \\ \eta &= \eta^h + \eta'. \end{aligned} \quad (2.14)$$

The coarse scales, denoted with superscript  $h$ , are represented on a given problem mesh. The test-function fine scales generate the so-called fine-scale equations, which give rise to the closure problem for the fine-scale solution fields. Following [11, 39, 68], it can be shown that the fine-scale equations are driven by the residuals of the coarse scales, which

6 *Y. Bazilevs, A. Korobenko, J. Yan, A. Pal, S.M.I. Gohari, and S. Sarkar*

motivates the following simple algebraic fine-scale model:

$$\mathbf{u}' = -\frac{\tau_{\text{SUPS}}}{\rho} \mathbf{r}_M(\mathbf{u}^h, p^h, \phi^h), \quad (2.15)$$

$$p' = -\rho \nu_{\text{LSIC}} r_C(\mathbf{u}^h), \quad (2.16)$$

$$\phi' = -\tau_{\text{SUPG}} r_A(\mathbf{u}^h, \phi^h), \quad (2.17)$$

Here  $\mathbf{r}_M$ ,  $r_C$ , and  $r_A$  are the residuals of the momentum, incompressibility, and advection-diffusion equations, respectively. They are defined as:

$$\begin{aligned} \mathbf{r}_M(\mathbf{u}^h, p^h, \phi^h) &= \rho \left( \frac{\partial \mathbf{u}^h}{\partial t} \Big|_{\hat{x}} + (\mathbf{u}^h - \hat{\mathbf{u}}^h) \cdot \nabla \mathbf{u}^h - \mathbf{f}^h \right) - \nabla \cdot \boldsymbol{\sigma}(\mathbf{u}^h, p^h) - \mathbf{b}^h, \\ r_C(\mathbf{u}^h) &= \nabla \cdot \mathbf{u}^h, \\ r_A(\mathbf{u}^h, \phi^h) &= \frac{\partial \phi^h}{\partial t} \Big|_{\hat{x}} + (\mathbf{u}^h - \hat{\mathbf{u}}^h) \cdot \nabla \phi^h - \nabla \cdot \kappa \nabla \phi^h - f^h. \end{aligned} \quad (2.18)$$

In Eqs. (2.15)-(2.17), parameters  $\tau_{\text{SUPS}}$ ,  $\nu_{\text{LSIC}}$ , and  $\tau_{\text{SUPG}}$  originate from stabilized methods in fluid mechanics. Their various definitions may be found in [11, 13, 15–18, 32, 37, 38, 68–75]. Here we provide the definitions employed in the present work:

$$\tau_{\text{SUPS}} = \left( \frac{4}{\Delta t^2} + (\mathbf{u}_1^h - \hat{\mathbf{u}}^h) \cdot \mathbf{G} (\mathbf{u}_1^h - \hat{\mathbf{u}}^h) + C_I \nu^2 \mathbf{G} : \mathbf{G} \right)^{-1/2}, \quad (2.19)$$

$$\nu_{\text{LSIC}} = (\text{tr} \mathbf{G} \tau_{\text{SUPS}})^{-1}, \quad (2.20)$$

$$\tau_{\text{SUPG}} = \left( \frac{4}{\Delta t^2} + (\mathbf{u}_1^h - \hat{\mathbf{u}}^h) \cdot \mathbf{G} (\mathbf{u}_1^h - \hat{\mathbf{u}}^h) + C_I \kappa^2 \mathbf{G} : \mathbf{G} \right)^{-1/2}, \quad (2.21)$$

where

$$\text{tr} \mathbf{G} = \sum_{i=1}^d G_{ii} \quad (2.22)$$

is the trace of the element metric tensor  $\mathbf{G}$ ,  $\Delta t$  is the time-step size, and  $C_I$  is a positive constant that derives from an appropriate element-wise inverse estimate (see, e.g., [76–78]).

Introducing the expressions given by Eqs. (2.15)-(2.17) into the coarse-scale variational equations generated by the coarse-scale test functions, the semi-discrete form of the ALE–VMS formulation for stratified flows may be stated as follows: Find  $\mathbf{u}^h$ ,  $p^h$ , and  $\phi^h$ , such

that, for all  $\mathbf{w}^h$ ,  $q^h$ , and  $\eta^h$ :

$$\begin{aligned}
 & \int_{\Omega} \mathbf{w}^h \cdot \rho \left( \frac{\partial \mathbf{u}^h}{\partial t} \Big|_{\hat{x}} + (\mathbf{u}^h - \hat{\mathbf{u}}^h) \cdot \nabla \mathbf{u}^h - \mathbf{f}^h \right) d\Omega - \int_{\Omega} \mathbf{w}^h \cdot \mathbf{b}^h d\Omega \\
 & + \int_{\Omega} \boldsymbol{\varepsilon}(\mathbf{w}^h) : 2\mu \boldsymbol{\varepsilon}(\mathbf{u}^h) d\Omega - \int_{\Gamma_h} \mathbf{w}^h \cdot \mathbf{h}^h d\Gamma + \int_{\Omega} q^h \nabla \cdot \mathbf{u}^h d\Omega \\
 & + \int_{\Omega} \eta^h \left( \frac{\partial \phi^h}{\partial t} \Big|_{\hat{x}} + (\mathbf{u}^h - \hat{\mathbf{u}}^h) \cdot \nabla \phi^h - f^h \right) d\Omega - \int_{\Omega} \nabla \eta^h \cdot \kappa \cdot \nabla \phi^h d\Omega - \int_{\Gamma_h^{\phi}} \eta^h h^h d\Gamma \\
 & + \sum_{e=1}^{N_{\text{el}}} \int_{\Omega^e} \tau_{\text{SUPS}} \left( (\mathbf{u}^h - \hat{\mathbf{u}}^h) \cdot \nabla \mathbf{w}^h + \frac{\nabla q^h}{\rho} \right) \cdot \mathbf{r}_M(\mathbf{u}^h, p^h, \phi^h) d\Omega \\
 & + \sum_{e=1}^{N_{\text{el}}} \int_{\Omega^e} \rho \nu_{\text{LSIC}} \nabla \cdot \mathbf{w}^h r_C(\mathbf{u}^h, p^h) d\Omega \\
 & - \sum_{e=1}^{N_{\text{el}}} \int_{\Omega^e} \tau_{\text{SUPS}} \mathbf{w}^h \cdot (\mathbf{r}_M(\mathbf{u}^h, p^h, \phi^h) \cdot \nabla \mathbf{u}^h) d\Omega \\
 & - \sum_{e=1}^{N_{\text{el}}} \int_{\Omega^e} \frac{\nabla \mathbf{w}^h}{\rho} : (\tau_{\text{SUPS}} \mathbf{r}_M(\mathbf{u}^h, p^h, \phi^h)) \otimes (\tau_{\text{SUPS}} \mathbf{r}_M(\mathbf{u}^h, p^h, \phi^h)) d\Omega \\
 & + \sum_{e=1}^{N_{\text{el}}} \int_{\Omega^e} \tau_{\text{SUPG}} (\mathbf{u}^h - \hat{\mathbf{u}}^h) \cdot \nabla \eta^h r_A(\mathbf{u}^h, \phi^h) d\Omega = 0, \tag{2.23}
 \end{aligned}$$

where  $N_{\text{el}}$  is the number of elements that subdivide the problem domain  $\Omega$ . We note that a comparable ST-VMS method was presented recently in [57] for thermo-fluid analysis, with application to a ground vehicle and its tires.

We augment the formulation given by Eq. (2.23) with weakly enforced essential boundary conditions [15] to improve boundary-layer solution accuracy. For this, the following

8 *Y. Bazilevs, A. Korobenko, J. Yan, A. Pal, S.M.I. Gohari, and S. Sarkar*

terms are added to the left-hand-side of Eq. (2.23):

$$\begin{aligned}
 & - \sum_{b=1}^{N_{\text{eb}}} \int_{\Gamma^b \cap \Gamma_g} \mathbf{w}^h \cdot \boldsymbol{\sigma}(\mathbf{u}^h, p^h) \mathbf{n} \, d\Gamma \\
 & - \sum_{b=1}^{N_{\text{eb}}} \int_{\Gamma^b \cap \Gamma_g} (2\mu \boldsymbol{\varepsilon}(\mathbf{w}^h) \mathbf{n} + q^h \mathbf{n}) \cdot (\mathbf{u}^h - \mathbf{g}^h) \, d\Gamma \\
 & - \sum_{b=1}^{N_{\text{eb}}} \int_{\Gamma^b \cap (\Gamma_g)^-} \mathbf{w}^h \cdot \rho((\mathbf{u}^h - \hat{\mathbf{u}}^h) \cdot \mathbf{n})(\mathbf{u}^h - \mathbf{g}^h) \, d\Gamma \\
 & + \sum_{b=1}^{N_{\text{eb}}} \int_{\Gamma^b \cap \Gamma_g} \tau_B \mathbf{w}^h \cdot (\mathbf{u}^h - \mathbf{g}^h) \, d\Gamma \\
 & - \sum_{b=1}^{N_{\text{eb}}} \int_{\Gamma^b \cap \Gamma_g^\phi} \eta^h \kappa \nabla \phi^h \cdot \mathbf{n} \, d\Gamma \\
 & - \sum_{b=1}^{N_{\text{eb}}} \int_{\Gamma^b \cap \Gamma_g^\phi} \kappa \nabla \phi^h \cdot \mathbf{n} (\phi^h - g^h) \, d\Gamma \\
 & - \sum_{b=1}^{N_{\text{eb}}} \int_{\Gamma^b \cap (\Gamma_g^\phi)^-} \eta^h ((\mathbf{u}^h - \hat{\mathbf{u}}^h) \cdot \mathbf{n}) (\phi^h - g^h) \, d\Gamma \\
 & + \sum_{b=1}^{N_{\text{eb}}} \int_{\Gamma^b \cap \Gamma_g^\phi} \tau_B^\phi \eta^h (\phi^h - g^h) \, d\Gamma
 \end{aligned} \tag{2.24}$$

where  $N_{\text{eb}}$  is the number of surface elements that subdivide the domain boundary,  $\Gamma_g$  and  $\Gamma_g^\phi$  are the subsets of the boundary with prescribed essential boundary conditions for the Navier–Stokes and advection–diffusion equations,  $(\Gamma_g)^-$  and  $(\Gamma_g^\phi)^-$  denote the “in-flow” parts of the essential boundary, and  $\mathbf{g}^h$  and  $g^h$  are the boundary condition values. In Eq. (2.24)  $\tau_B$  and  $\tau_B^\phi$  are the boundary stabilization or penalty parameters defined from considerations of stability, optimal convergence, and connection with near-wall modeling (i.e., wall functions). For more details on weakly enforced boundary conditions and definition of stabilization parameters the reader is referred to [16–18].

### 2.3. Additional VMS modeling terms and stabilization parameters

In the VMS framework, coupling between Navier–Stokes and advection–diffusion equations brought about by the Boussinesq approximation gives rise to additional modeling terms. In particular, it can be shown that the  $x_3$ -component of the linear-momentum equation and incompressibility constraint are coupled with the residual of the advection–diffusion equation, and the following terms may be added to the left-hand-side of

Eq. (2.23):

$$+ \sum_{e=1}^{N_{el}} \int_{\Omega^e} \left( (\mathbf{u}^h - \hat{\mathbf{u}}^h) \cdot \frac{\partial w_3^h}{\partial \mathbf{x}} + \frac{1}{\rho} \frac{\partial q^h}{\partial x_3} \right) \bar{\tau} r_A(\mathbf{u}^h, \phi^h) \, d\Omega. \quad (2.25)$$

The stabilization parameter  $\bar{\tau}$  may be obtained following the developments of stabilized methods for advective–diffusive systems presented in [79–81], which gives a possible candidate for  $\bar{\tau}$ ,

$$\bar{\tau} = -\frac{a_2}{a_1 \sqrt{a_3} + a_3 \sqrt{a_1}}, \quad (2.26)$$

where  $a_i$ 's are given by

$$\begin{aligned} a_1 &= \frac{4}{\Delta t^2} + (\mathbf{u}^h - \hat{\mathbf{u}}^h) \cdot \mathbf{G}(\mathbf{u}^h - \hat{\mathbf{u}}^h) + C_I \nu^2 \mathbf{G} : \mathbf{G}, \\ a_2 &= \frac{4}{\Delta t} Ri, \\ a_3 &= \frac{4}{\Delta t^2} + (\mathbf{u}^h - \hat{\mathbf{u}}^h) \cdot \mathbf{G}(\mathbf{u}^h - \hat{\mathbf{u}}^h) + C_I \kappa^2 \mathbf{G} : \mathbf{G}, \end{aligned} \quad (2.27)$$

and where  $Ri = 1/Fr^2$  is the so-called Richardson number, a non dimensional parameter that characterizes the degree of stratification in the flow. Although the numerical examples presented in the following sections do not make use of these additional terms, it may be of interest to assess their importance in future studies.

### 3. Numerical Examples

#### 3.1. Internal gravity waves in a density-stratified fluid

This example deals with generation of internal gravity waves in laminar flow. Internal gravity waves occur in density-stratified fluids under the restoring force of gravity. The dispersion relation for such waves is

$$\omega = N \cos(\theta), \quad (3.1)$$

where  $N$  is the buoyancy (or Brunt–Vaisala) frequency,  $\omega$  is the wave frequency, and  $\theta$  is the angle between the fluid particle velocity and vertical direction (see, e.g., [65, 66] for details). The dispersion relation clearly shows that the maximum frequency of propagating internal waves is the buoyancy frequency  $N$ . The generation of internal gravity waves was demonstrated in several laboratory experiments [82, 83]. The waves may be generated by a small disturbance in the fluid (e.g., by means of an oscillating cylinder), and visualized using a so-called schlieren system [82, 83].

Here the problem is defined numerically and is set up using a cylindrical domain with length  $L = 1$  and radius  $R = 5$ . The fluid occupying the domain has uniform buoyancy frequency  $N = 1$  and is forced along the cylinder axis in the vertical direction (i.e., direction of density stratification) at a frequency  $\omega = 0.71$ . Although the problem is computed in 3D, it is constrained to produce a 2D response. On the lateral boundaries we set zero traction

10 *Y. Bazilevs, A. Korobenko, J. Yan, A. Pal, S.M.I. Gohari, and S. Sarkar*

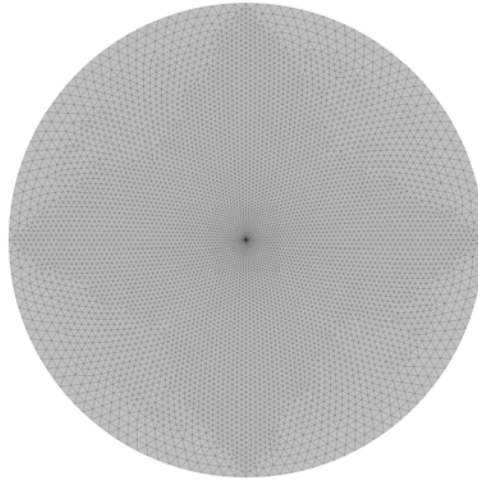


Fig. 1. Internal gravity waves. Problem mesh.

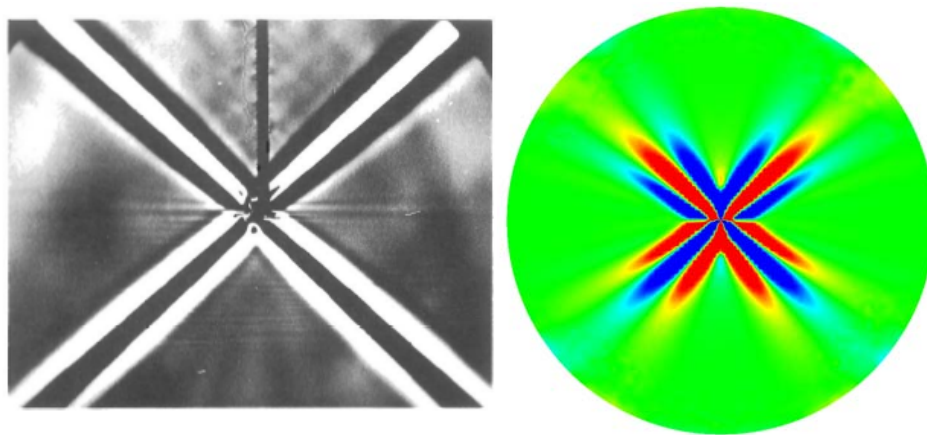


Fig. 2. Internal gravity waves. Left: Visualization of experimental results from [65]. Right: Vertical velocity gradient magnitude from the present computation.

boundary conditions and scalar flux boundary conditions that are consistent with the background density stratification. The problem is computed on a mesh of 304,240 tetrahedral elements (see Figure 1), and the vertical-velocity gradient magnitude is visualized in Figure 2. Experimental observations from [65] are also plotted for comparison. The velocity gradient exhibits “streaks” at  $45^\circ$  to the stratification direction, a result that is consistent with the analytical dispersion relation given by Eq. (3.1) and experimental observations.

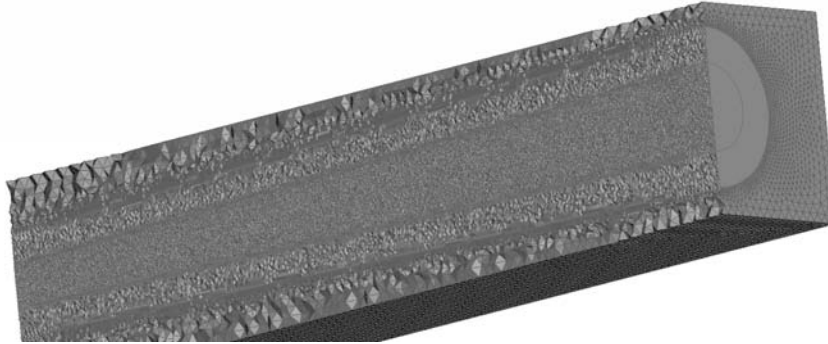


Fig. 3. Spatially evolving wake. Mesh of the problem domain with refined regions.

	Num. of nodes	Num. of elements
Mesh	3,815,319	22,547,731

Table 1. Spatially evolving wake. Problem mesh statistics.

Inner cone	Outer cone	Outer box
0.08	0.1	0.25

Table 2. Spatially evolving wake. Element size employed in the different regions of the problem domain.

### 3.2. Spatially evolving self-propelled wake in a density-stratified fluid

We compute a spatially evolving wake in a density-stratified fluid at  $Re = 15,000$ ,  $Fr = 3$ , and  $Pr = 1$ . The flow is turbulent and the problem setup corresponds to a recent DNS study of a self-propelled wake with 50% mean kinetic energy and a given energy spectrum [4]. In what follows we refer to this case as SP50.

#### 3.2.1. Problem setup and mesh

The problem computational domain is defined as follows. The outer boundary is a box with dimensions  $22.125D \times 14.482D \times 65D$ , where  $D$  is the characteristic length. In order to get the desired non-dimensional values of  $Re$ ,  $Fr$ , and  $Pr$ , the problem parameters are set as follows:  $D = 1$ ,  $U = 1$  (background inlet velocity),  $\rho_0 = 1$ ,  $\mu = 1/15,000$ ,  $N = 1/3$ , and  $\kappa = 1/15,000$ . At the inlet, the inflow velocity and density are imposed strongly. The inflow data comes from a separate temporally evolving wake simulation described in detail in the next section. At the outlet, zero traction and zero scalar flux boundary conditions are imposed. On the lateral boundaries, no penetration and zero tangential traction bound-

12 *Y. Bazilevs, A. Korobenko, J. Yan, A. Pal, S.M.I. Gohari, and S. Sarkar*

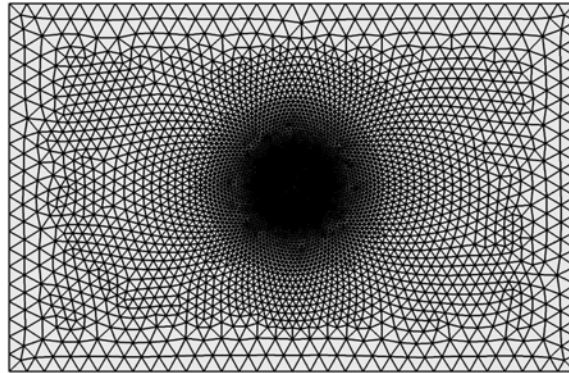


Fig. 4. Spatially evolving wake. Triangular mesh of the inflow boundary.

ary conditions are set for the Navier–Stokes equations, and flux boundary conditions consistent with the background density stratification are imposed for the advection–diffusion equation. Two cone-shaped mesh refinement zones are defined to better capture the turbulent wake features. At the inlet, the radii of the inner and outer cones are  $2.5D$  and  $3.5D$ , respectively. At the outlet, the radii of the inner and outer cones are  $3.5D$  and  $6D$ , respectively. These two refined regions are sufficient to contain the expanding wake. The problem tetrahedral mesh with refined regions is depicted in Figure 3. The mesh statistics are summarized in Tables 1 and 2. The time step is set to  $\Delta t = 0.002$ , and the simulation is performed for 520 non-dimensional time units, which corresponds to eight flow-throughs.

### 3.2.2. Turbulent wake inflow generation

In order to generate the inflow data that is used for the present simulation, a standalone computation of a temporally evolving wake is carried out using a structured-grid finite-volume technique. The computational procedure and set-up of this auxiliary computation is identical to that employed in the DNS of [4]. Solution data generated by this auxiliary simulation is “fed” into the computational domain of the present spatial simulation as inflow boundary conditions. To impose stratified turbulent inflow conditions for the spatial simulation, the inflow velocity and density data are transferred from the structured grid to the unstructured triangular mesh. Figure 4 shows the unstructured triangular mesh at the inlet of the spatial domain. On the inlet plane, the unstructured mesh is clustered in the inner region to have a more accurate representation of the flow features. The triangular mesh becomes coarser near the lateral boundaries since no significant velocity and density fluctuations are present in this location, and thus do not need to be resolved. To transfer the velocity and density data between the two meshes, the  $L_2$ -projection technique is employed. Figure 5 shows the the velocity magnitude before and after the  $L_2$ -projection. Note that all the scales are preserved in the region near the center of the inflow face. The  $L_2$ -projection is performed for every plane generated by the auxiliary simulation. Piecewise linear interpolation in time is

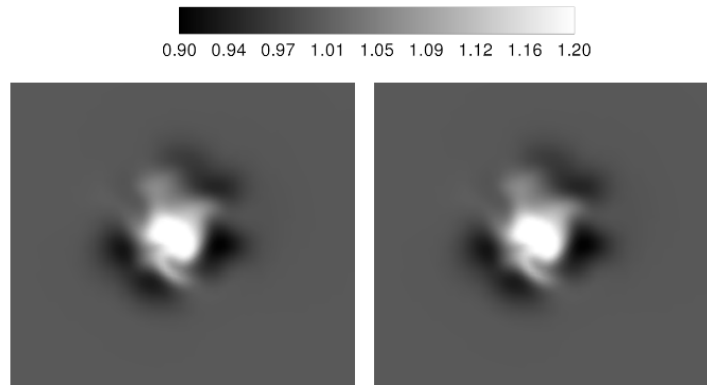


Fig. 5. Spatially evolving wake. Velocity magnitude on the inflow plane. Left: before projection. Right: after projection.

assumed when the turbulent inflow field is needed in the intermediate locations between the planes of the auxiliary simulation.

### 3.2.3. Flow features and statistics

We present wake flow features and statistics obtained in the present computation and use the DNS data from [4] as reference. Figure 6 shows the contours of the mean stream-wise velocity at several cuts along the flow direction. The top figure shows the mean velocity profile right near the inlet. The profile is axisymmetric and contains positive and negative velocity lobes (i.e., thrust and drag lobes). The middle and bottom figures depict the subsequent anisotropic growth of the wake that occurs mainly in the horizontal direction. The negative velocity lobes eventually vanish along the horizontal direction, but remain along the vertical direction over the entire stream-wise extent of the domain. The reason for the survival of the negative lobes is the effect of buoyancy that inhibits vertical mixing of momentum. The wave field associated with the self-propelled wake is shown via the contours of horizontal vorticity at various downstream locations in Figure 7. The current simulation, although performed on a much coarser mesh, is able to replicate the gravity wave patterns present in the DNS computation. In addition, Figure 7 shows that, at later time, the central region of the wake has multiple coherent layers of stream-wise vorticity. These correspond to regions of large vertical shear between the adjacent “pancake” eddies. Figure 8 shows vorticity isosurfaces colored by flow speed. The wake anisotropic growth along the stream-wise direction can be clearly observed. The figure also illustrates the complexity of the underlying turbulent flow phenomena, and underscores the necessity to develop and use stable and accurate numerical techniques for this problem class. The plane-integrated statistics, namely, production and turbulent kinetic energy (see [7] for definition of these standard turbulent-flow quantities), are plotted as a function of the stream-wise variable in

14 *Y. Bazilevs, A. Korobenko, J. Yan, A. Pal, S.M.I. Gohari, and S. Sarkar*

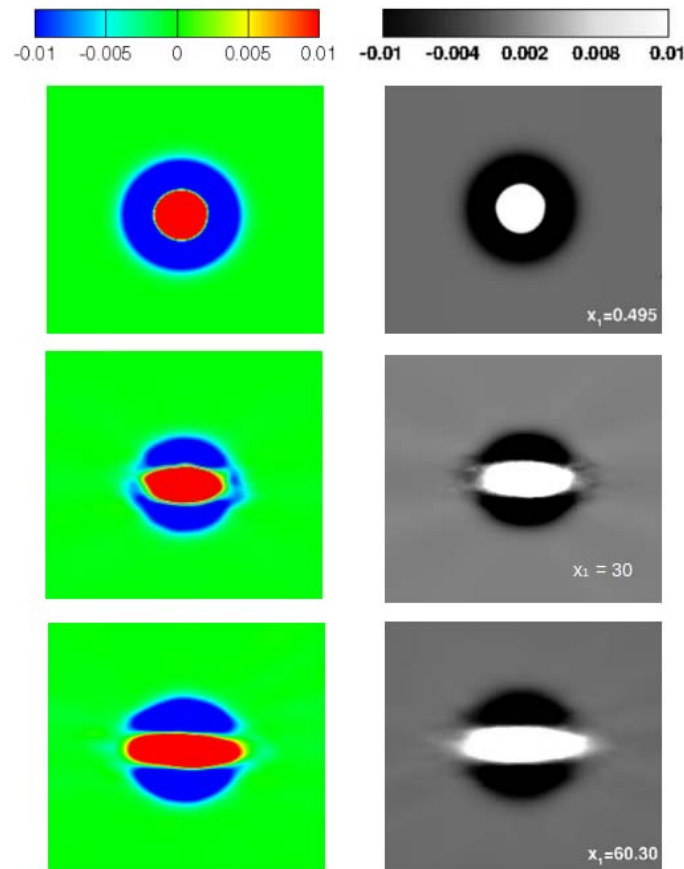


Fig. 6. Spatially evolving wake. Mean velocity contours at several streamwise cuts. Left: Present computation; Right: DNS data from [4].

Figure 9. Good agreement with the DNS data is observed, especially further downstream of the inlet. However, in the region where the stream-wise coordinate ranges from  $x_1 = 15$  to  $x_1 = 25$ , there are some differences in the turbulent production, which may be attributable to lower resolution of the present computation relative to the DNS.

### 3.3. *Wind-turbine rotor in an atmospheric boundary layer*

In this section we investigate the behavior of a full-scale offshore wind-turbine rotor placed in a thermally stratified ABL. For this we first perform a standalone 3D large-eddy simulation (LES) computation of an ABL on a domain which is a cube with dimension 400 m and uniform grid size of 5 m. The LES [84, 85] employs a mixed spectral-finite difference algorithm and dynamic eddy viscosity and eddy diffusivity models to simulate stratified

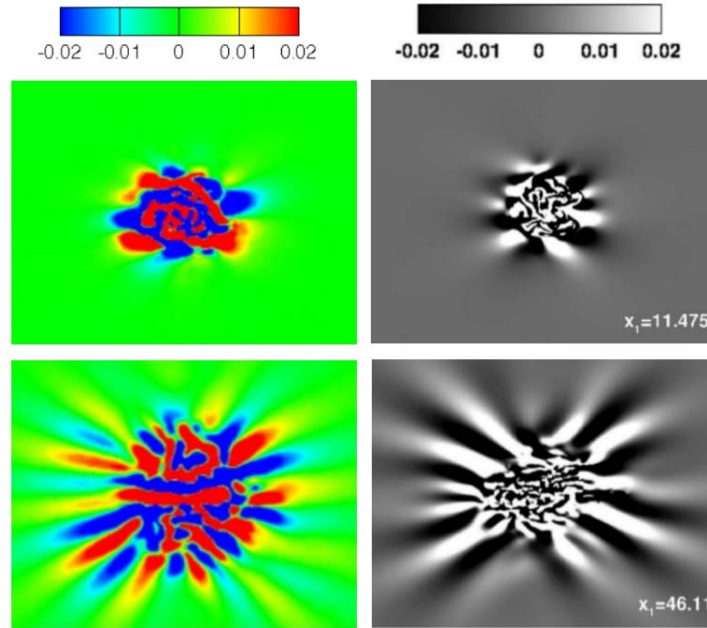


Fig. 7. Spatially evolving wake. Instantaneous internal gravity wave field visualized by snapshots of streamwise vorticity at several streamwise cuts. Left: Present computation; Right: DNS data from [4].

flows. The reference temperature is set to 260 K, and a vertical temperature gradient of 0.01 K/m is prescribed starting at 100 m above ground. The geostrophic wind speed is set to 8 m/s, and the Coriolis parameter  $f_c = 1.39 \times 10^{-4} \text{ s}^{-1}$  is employed in the computation. The computational set-up is similar to that in [6]. The data from the LES computation is used as inlet boundary conditions for the ALE-VMS wind-turbine rotor computation, which is described in what follows.

The problem domain is a cylinder that is 240 m in length and diameter. A 5 MW wind-turbine rotor with diameter of 120 m, analyzed earlier in [19–21, 25, 41–43, 86], is placed in the cylindrical domain. The rotor spins with a prescribed, constant angular velocity, and no sliding interface or FSI coupling are employed in the present computation. The problem domain is discretized using triangular prisms in the boundary layer region and tetrahedra elsewhere, resulting in 7,431,784 linear elements (see Figure 10). The boundary-layer mesh design is based on that reported in [21], where an FSI simulation of a full offshore wind turbine with yawing motion was performed using a newly proposed moving sliding-interface technique. The mesh is refined in the inner region of the domain in order to better resolve the ABL turbulent flow that impacts the rotor.

To impose turbulent inlet velocity and temperature boundary conditions, the solution data is transferred from the structured grid of the LES simulation to the unstructured mesh of the spinning rotor problem. The spinning rotor domain is immersed into a larger LES

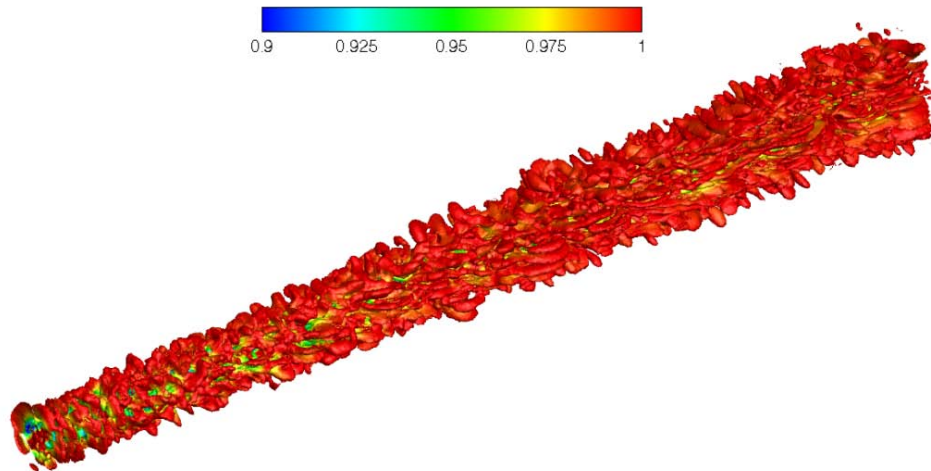


Fig. 8. Spatially evolving wake. Isosurfaces of vorticity colored by flow speed at a time instant.

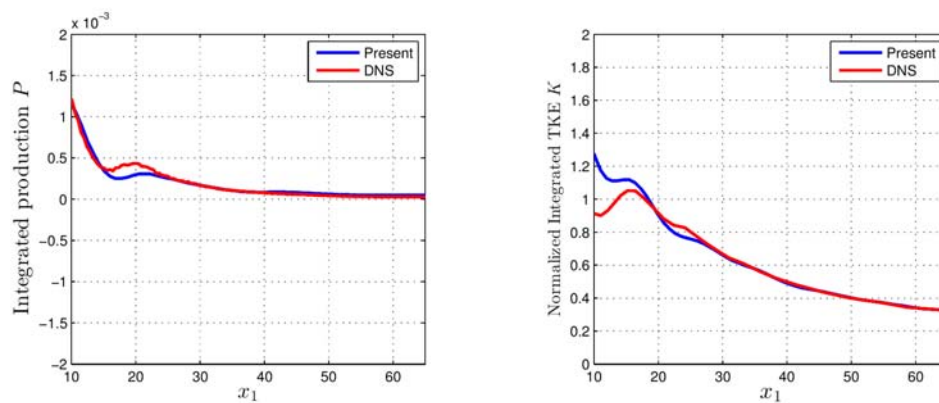


Fig. 9. Spatially evolving wake. Left: Plane-integrated turbulent production as a function of streamwise coordinate; Right: Normalized, plane-integrated turbulent kinetic energy. (See [7] for definition of these standard turbulent-flow quantities.) DNS data from [4] is also shown.

domain and the velocity and temperature data assigned to the nodes of the cylinder inflow plane and lateral boundaries is obtained by interpolating the finite-difference solution (see Figure 11). At the outlet, traction boundary conditions are prescribed. The distribution of outlet traction is obtained by computing the problem on a non-spinning domain, with

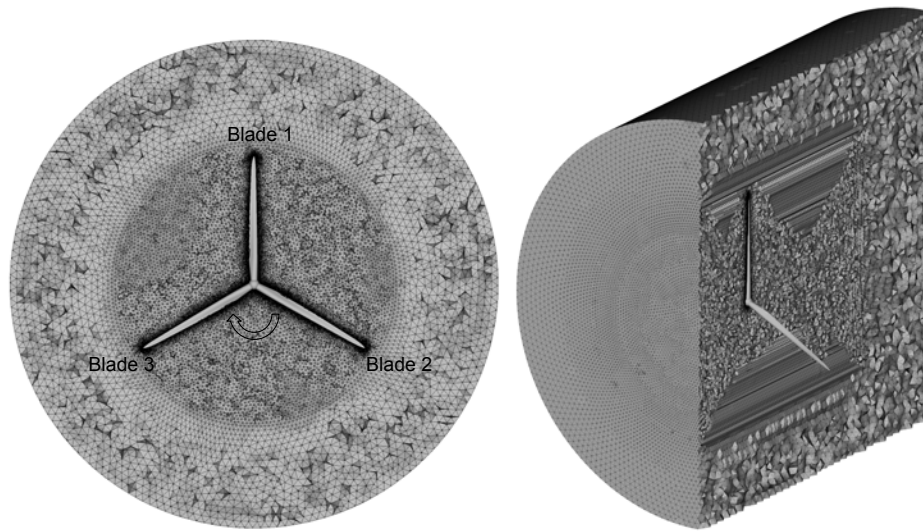


Fig. 10. Wind-turbine rotor in an ABL. Mesh of computational domain in 2D and 3D views. The rotor blades are numbered clockwise and arrow indicates rotation direction.

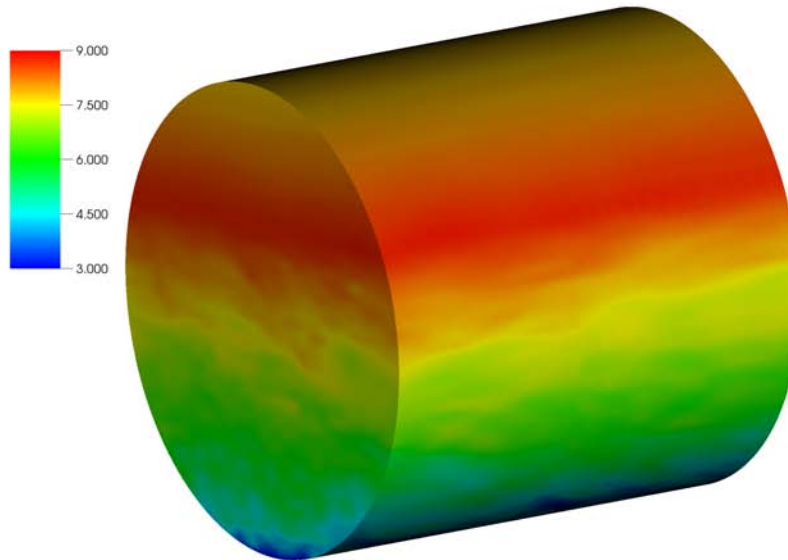


Fig. 11. Wind-turbine rotor in an ABL. Velocity (in m/s) initial and boundary conditions obtained by “immersing” the cylindrical spinning domain into a larger LES domain and performing interpolation of the LES solution.

18 *Y. Bazilevs, A. Korobenko, J. Yan, A. Pal, S.M.I. Gohari, and S. Sarkar*

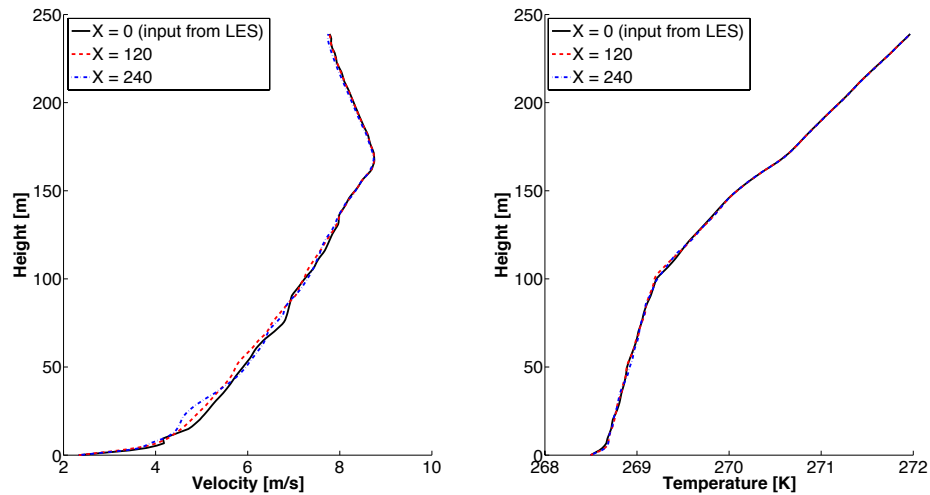


Fig. 12. Wind-turbine rotor in an ABL. Mean velocity and temperature as a function of the vertical coordinate.

the rotor removed, and with zero outlet traction boundary conditions. The inlet tractions produced as a result of this computation are assigned as outlet traction boundary conditions in the rotating-domain computation. We note that a similar concept was used in [57] for detailed thermo-fluid analysis of the rear tires of a ground vehicle. In [57], the thermo-fluid computation over the global domain (including all the tires) with a reasonable mesh refinement is followed by a higher-resolution computation over the local domain containing the rear set of tires, with the boundary and initial conditions coming from the data computed over the global domain. The data computed over the global domain is stored using the data compression method introduced in [87].

Figure 12 shows the mean velocity and temperature as a function of the vertical coordinate, at  $x_1 = 120$  m and  $x_1 = 240$  m locations downstream of the inflow. The results are compared to the mean of the velocity and temperature imposed on the inlet, which corresponds to the interpolated LES data. The two profiles are very close, suggesting that ALE-VMS and LES ABL are mutually consistent.

For the wind turbine simulation the rotor speed is set to 9 rpm. This rotor speed chosen gives the optimal tip-speed ratio for 8 m/s wind speed [88], which is also the geostrophic wind speed used in the computation. The time-step size of  $2.0 \times 10^{-4}$  s is employed. The flow is initialized using the LES data interpolated to the interior of the rotor mesh, and the computation is started impulsively. Figure 13 shows vorticity isosurfaces at  $t = 8.5$  s. Due to the presence of the inversion layer, tip vortices travel with different speeds, faster near the top and slower near the bottom of the domain. As a result, the perfect helical pattern of tip vortices, which is expected in the case of uniform flow, is no longer present. As the rotor turns and blades travel in and out of the inversion layer, they introduce a certain amount

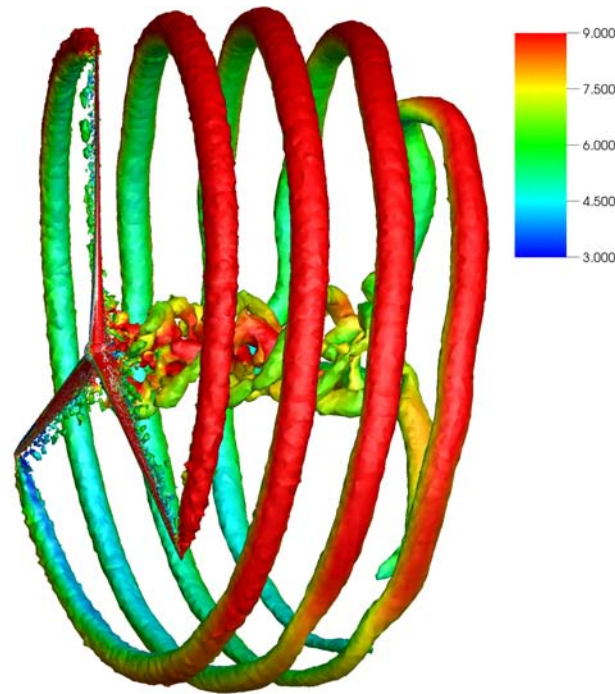


Fig. 13. Wind-turbine rotor in an ABL. Vorticity isosurfaces colored by flow speed (in m/s) at  $t = 8.5$  s.

of mixing in the flow (see Figure 14). This inversion-layer mixing propagates downstream and gives a complex and largely unstudied wake behavior.

The next set of figures examine the time-dependent rotor loads. The rotor-thrust time history is shown in Figure 15, where thrust is plotted for each individual blade (see Figure 10 for blade numbering). The presence of ABL produces an 18% fluctuation in the thrust load during the cycle. Figure 16 shows rotor-torque time history for each individual blade, which exhibits an even larger variation during the cycle. These fluctuations are significant and, to our knowledge, are reported for the first time for a full-scale rotor in an ABL. The time history of the total rotor torque is shown in Figure 17. Adding the torques from all three blades appears to remove the fluctuation in the signal. The result is compared with the torque data from [88] for uniform inflow of 8 m/s. The present computation predicts a lower torque value since the average wind speed the rotor sees is less than 8 m/s (see Figure 12).

#### 4. Conclusions

We developed an ALE-VMS formulation aimed at the simulation of stratified flows on moving domains. The formulation couples the Navier-Stokes equations of incompressible flows with the Boussinesq approximation, and a scalar advection-diffusion equation for the

20 *Y. Bazilevs, A. Korobenko, J. Yan, A. Pal, S.M.I. Gohari, and S. Sarkar*

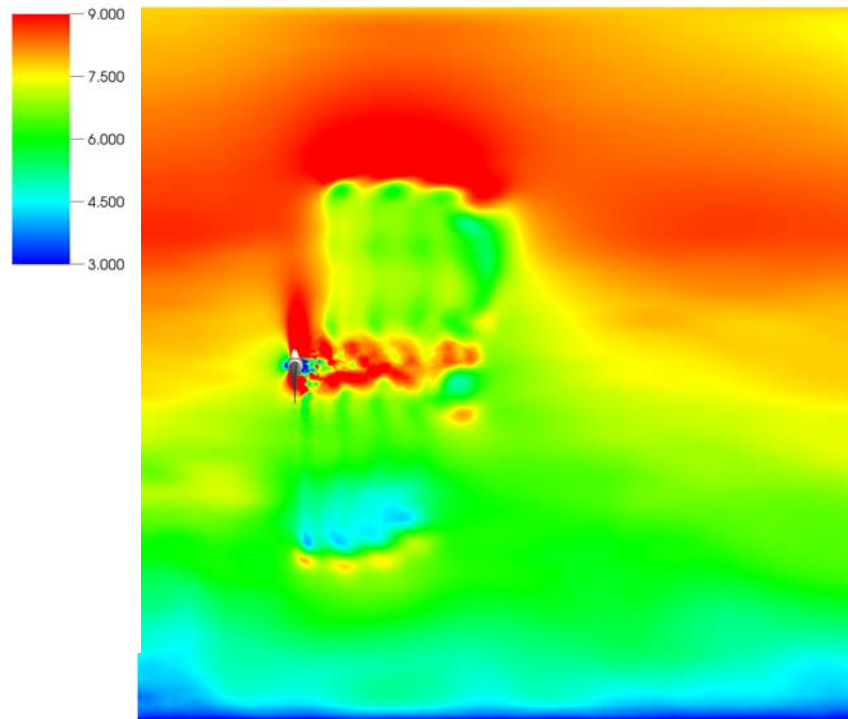


Fig. 14. Wind-turbine rotor in an ABL. Flow speed (in m/s) contours on a 2D slice of the problem domain showing mixing of the inversion layer in the rotor wake.

density or temperature field. The proposed formulation was tested on three examples and showed good agreement with experimental results and DNS simulations reported by other researchers. In the last example we simulated a full-scale 5 MW offshore wind-turbine rotor in a thermally-stratified ABL and observed significant variations in the rotor-blade thrust and torque loads during the rotation cycle. These results, presented for the first time in the open literature, indicate that stratification strongly affects the transient rotor loads, and should be considered in the structural and FSI analyses of offshore wind-turbine blades, especially for the prediction of fatigue damage and remaining useful life of these structures.

In the near future we plan to combine the newly developed ALE-VMS formulation of stratified flows with our full-machine FSI framework to simulate wind turbines operating in an ABL. These simulations will likely produce more realistic structural mechanics response of the blades, and will give us better understanding of the turbulent wake structures created downstream the turbine. As mentioned at the end of Section 2, the Boussinesq term in the linear-momentum balance equation gives rise to additional residual-based terms. Although not investigated in the present work, these modeling terms may play an important role, and will be considered in the future implementations of the ALE-VMS framework. Finally, in the present work low-order FEM was employed in the simulations. The use of

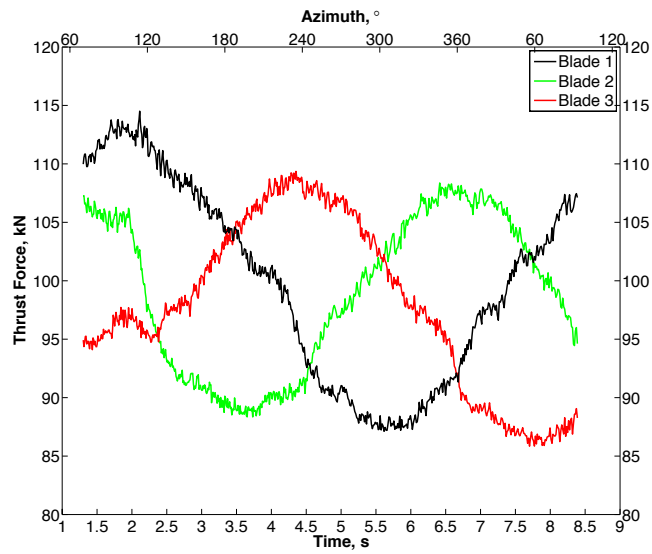


Fig. 15. Wind-turbine rotor in an ABL. Time history of the thrust force acting on each blade.

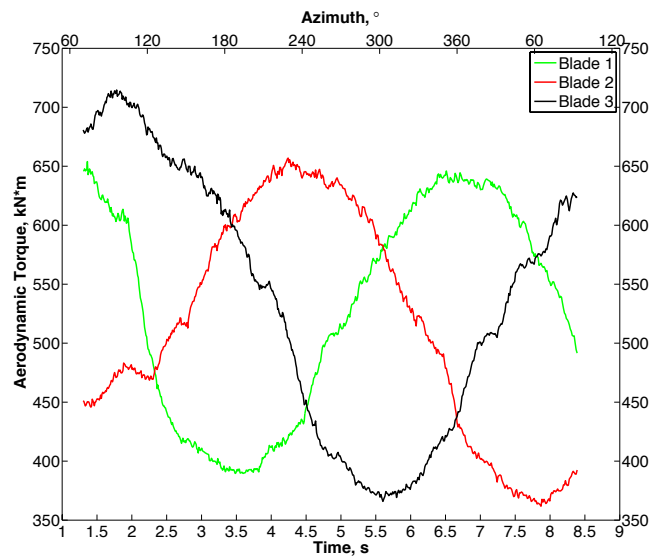


Fig. 16. Wind-turbine rotor in an ABL. Time history of the aerodynamic torque acting on each blade.

22 *Y. Bazilevs, A. Korobenko, J. Yan, A. Pal, S.M.I. Gohari, and S. Sarkar*

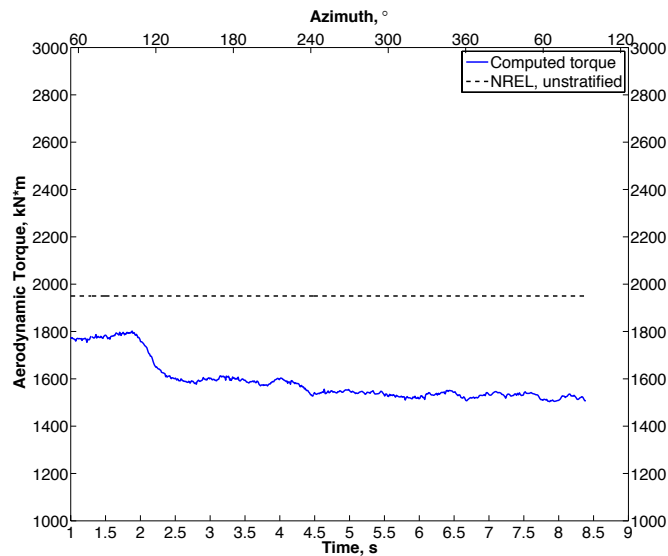


Fig. 17. Wind-turbine rotor in an ABL. Time history of the total aerodynamic torque. Torque data from [88] for uniform inflow of 8 m/s is also shown.

Isogeometric Analysis (IGA) [89, 90] in combination with the proposed ALE–VMS formulation will likely produce further improvements in the per-degree-of-freedom accuracy for stratified flow simulations due to the higher-order accuracy and smoothness of the underlying discretizations in IGA.

### Acknowledgments

This work was supported by the NSF Award CBET-1306869 and the NSF CAREER Award. This support is gratefully acknowledged.

### References

1. M. Bonnier and O. Eiff. Experimental investigation of the collapse of a turbulent wake in a stably stratified fluid. *Phys. Fluids*, 14:791–801, 2002.
2. G. Spedding. The evolution of initially turbulent bluff-body wakes at high internal froude number. *Journal of Fluid Mechanics*, 337:283–301, 1997.
3. R. Pasquetti. Temporal/spatial simulation of the stratified far wake of a sphere. *Computers and Fluids*, 40:179–187, 2011.
4. A. Pal, M.B. de Stadler, and S. Sarkar. The spatial evolution of fluctuations in a self-propelled wake compared to a patch of turbulence. *Physics of Fluids*, 25(9):095106, 2013.
5. M. B. De Stadler and S. Sarkar. Simulation of a propelled wake with moderate excess momentum in a stratified fluid. *Journal of Fluid Mechanics*, 692:28–52, 2012.
6. R.J. Beare, M.K. Macvean, A.A.M. Holtslag, J. Cuxart, I. Esau, J.-C. Golaz, M.A. Jimenez, M. Khairoutdinov, B. Kosovic, D Lewellen, T.S. Lund, J.K. Lundquist, A. McCabe, A.F. Moene,

- Y. Noh, S. Raasch, and P. Sullivan. An intercomparison of large-eddy simulations of the stable boundary layer. *Boundary-Layer Meteor.*, 118:247–272, 2006.
7. S. B. Pope. *Turbulent Flows*. Cambridge University Press, Cambridge, 2000.
  8. F. Porte-Agel, Y.-T. Wu, H. Lu, and R. J. Conzemius. Large-eddy simulation of atmospheric boundary layer flow through wind turbines and wind farms. *J. Wind Eng. Ind. Aerodyn.*, 99:154–168, 2011.
  9. N. Troldborg, J. N. Sorensen, R. F. Mikkelsen, and N. N. Sorensen. A simple atmospheric boundary layer model applied to large eddy simulations of wind turbine wakes. *J. Wind Energy*, 17:641–655, 2011. DOI: <http://dx.doi.org/10.1002/we.1608>.
  10. S. Lee, M. Churchfield, P. Moriarty, J. Jonkman, and J. Michalakes. Atmospheric and wake turbulence impacts on wind turbine fatigue loading. Technical Report NREL/CP-5000-53567, National Renewable Energy Laboratory, 2011.
  11. Y. Bazilevs, V. M. Calo, J. A. Cottrel, T. J. R. Hughes, A. Reali, and G. Scovazzi. Variational multiscale residual-based turbulence modeling for large eddy simulation of incompressible flows. *Computer Methods in Applied Mechanics and Engineering*, 197:173–201, 2007.
  12. T. J. R. Hughes, W. K. Liu, and T. K. Zimmermann. Lagrangian–Eulerian finite element formulation for incompressible viscous flows. *Computer Methods in Applied Mechanics and Engineering*, 29:329–349, 1981.
  13. Y. Bazilevs, V. M. Calo, T. J. R. Hughes, and Y. Zhang. Isogeometric fluid–structure interaction: theory, algorithms, and computations. *Computational Mechanics*, 43:3–37, 2008.
  14. I. Akkerman, Y. Bazilevs, V. M. Calo, T. J. R. Hughes, and S. Hulshoff. The role of continuity in residual-based variational multiscale modeling of turbulence. *Computational Mechanics*, 41:371–378, 2008.
  15. Y. Bazilevs and T. J. R. Hughes. Weak imposition of Dirichlet boundary conditions in fluid mechanics. *Computers and Fluids*, 36:12–26, 2007.
  16. Y. Bazilevs, C. Michler, V. M. Calo, and T. J. R. Hughes. Weak Dirichlet boundary conditions for wall-bounded turbulent flows. *Computer Methods in Applied Mechanics and Engineering*, 196:4853–4862, 2007.
  17. Y. Bazilevs, C. Michler, V. M. Calo, and T. J. R. Hughes. Isogeometric variational multiscale modeling of wall-bounded turbulent flows with weakly enforced boundary conditions on unstretched meshes. *Computer Methods in Applied Mechanics and Engineering*, 199:780–790, 2010.
  18. Y. Bazilevs and I. Akkerman. Large eddy simulation of turbulent Taylor–Couette flow using isogeometric analysis and the residual–based variational multiscale method. *Journal of Computational Physics*, 229:3402–3414, 2010.
  19. Y. Bazilevs, M.-C. Hsu, I. Akkerman, S. Wright, K. Takizawa, B. Henicke, T. Spielman, and T. E. Tezduyar. 3D simulation of wind turbine rotors at full scale. Part I: Geometry modeling and aerodynamics. *International Journal for Numerical Methods in Fluids*, 65:207–235, 2011.
  20. Y. Bazilevs, M.-C. Hsu, J. Kiendl, R. Wüchner, and K.-U. Bletzinger. 3D simulation of wind turbine rotors at full scale. Part II: Fluid–structure interaction modeling with composite blades. *International Journal for Numerical Methods in Fluids*, 65:236–253, 2011.
  21. Y. Bazilevs, A. Korobenko, X. Deng, and J. Yan. Novel structural modeling and mesh moving techniques for advanced FSI simulation of wind turbines. *International Journal for Numerical Methods in Engineering*, 2014. Published online. DOI: 10.1002/nme.4738.
  22. Y. Bazilevs, K. Takizawa, T.E. Tezduyar, M.-C. Hsu, N. Kostov, and S. McIntyre. Aerodynamic and FSI analysis of wind turbines with the ALE-VMS and ST-VMS methods. *Archives of Computational Methods in Engineering*, 21:359–398, 2014.
  23. A. Korobenko, M.-C. Hsu, I. Akkerman, J. Tippmann, and Y. Bazilevs. Structural mechanics modeling and fsi simulation of wind turbines. *Mathematical Models and Methods in Applied Sciences*, 23:249–272, 2013. DOI: 10.1142/S0218202513400034.

- 24 Y. Bazilevs, A. Korobenko, J. Yan, A. Pal, S.M.I. Gohari, and S. Sarkar
24. A. Korobenko, M.-C. Hsu, I. Akkerman, and Y. Bazilevs. Aerodynamic simulation of vertical-axis wind turbines. *Journal of Applied Mechanics*, 81(2), 021011, 2013.
25. M.-C. Hsu and Y. Bazilevs. Fluid–structure interaction modeling of wind turbines: Simulating the full machine. *Computational Mechanics*, 50:821–833, 2012.
26. Y. Bazilevs, M.-C. Hsu, K. Takizawa, and T. E. Tezduyar. ALE-VMS and ST-VMS methods for computer modeling of wind-turbine rotor aerodynamics and fluid–structure interaction. *Mathematical Models and Methods in Applied Sciences*, 22(supp02):1230002, 2012.
27. B. Augier, J. Yan, A. Korobenko, J. Czarnowski, G. Ketterman, and Y. Bazilevs. Experimental and numerical FSI study of compliant hydrofoils. *Computational Mechanics*, 2014. Published online. DOI:10.1007/s00466-014-1090-5.
28. K. Takizawa, Y. Bazilevs, and T. E. Tezduyar. Space–time and ALE-VMS techniques for patient-specific cardiovascular fluid–structure interaction modeling. *Archives of Computational Methods in Engineering*, 19:171–225, 2012.
29. K. Takizawa, Y. Bazilevs, T. E. Tezduyar, C. C. Long, A. L. Marsden, and K. Schjodt. ST and ALE-VMS methods for patient-specific cardiovascular fluid mechanics modeling. *Mathematical Models and Methods in Applied Sciences*, 24:2437–2486, 2014.
30. M.-C. Hsu, D. Kamensky, Y. Bazilevs, M. S. Sacks, and T. J. R. Hughes. Fluid–structure interaction analysis of bioprosthetic heart valves: significance of arterial wall deformation. *Computational Mechanics*, 54:1055–1071, 2014.
31. D. Kamensky, M.-C. Hsu, D. Schillinger, J.A. Evans, A. Aggarwal, Y. Bazilevs, M.S. Sacks, and T.J.R. Hughes. An immersogeometric variational framework for fluid–structure interaction: Application to bioprosthetic heart valves. *Computer Methods in Applied Mechanics and Engineering*, 284:1005–1053, 2015.
32. K. Takizawa and T. E. Tezduyar. Multiscale space–time fluid–structure interaction techniques. *Computational Mechanics*, 48:247–267, 2011.
33. K. Takizawa and T. E. Tezduyar. Space–time fluid–structure interaction methods. *Mathematical Models and Methods in Applied Sciences*, 22(supp02):1230001, 2012.
34. T. E. Tezduyar. Stabilized finite element formulations for incompressible flow computations. *Advances in Applied Mechanics*, 28:1–44, 1992.
35. T. E. Tezduyar, M. Behr, and J. Liou. A new strategy for finite element computations involving moving boundaries and interfaces – the deforming-spatial-domain/space–time procedure: I. The concept and the preliminary numerical tests. *Computer Methods in Applied Mechanics and Engineering*, 94(3):339–351, 1992.
36. T. E. Tezduyar, M. Behr, S. Mittal, and J. Liou. A new strategy for finite element computations involving moving boundaries and interfaces – the deforming-spatial-domain/space–time procedure: II. Computation of free-surface flows, two-liquid flows, and flows with drifting cylinders. *Computer Methods in Applied Mechanics and Engineering*, 94(3):353–371, 1992.
37. T. E. Tezduyar. Computation of moving boundaries and interfaces and stabilization parameters. *International Journal for Numerical Methods in Fluids*, 43:555–575, 2003.
38. T. E. Tezduyar and S. Sathe. Modeling of fluid–structure interactions with the space–time finite elements: Solution techniques. *International Journal for Numerical Methods in Fluids*, 54:855–900, 2007.
39. Y. Bazilevs, K. Takizawa, and T. E. Tezduyar. *Computational Fluid–Structure Interaction: Methods and Applications*. Wiley, 2013.
40. K. Takizawa, Y. Bazilevs, T. E. Tezduyar, M.-C. Hsu, O. Oiseth, K. M. Mathisen, N. Kostov, and S. McIntyre. Engineering analysis and design with ALE-VMS and Space–Time methods. *Archives of Computational Methods in Engineering*, 21:481–508, 2014.
41. K. Takizawa, B. Henicke, T. E. Tezduyar, M.-C. Hsu, and Y. Bazilevs. Stabilized space–time computation of wind-turbine rotor aerodynamics. *Computational Mechanics*, 48:333–344, 2011.
42. K. Takizawa, B. Henicke, D. Montes, T. E. Tezduyar, M.-C. Hsu, and Y. Bazilevs. Numerical-

- performance studies for the stabilized space-time computation of wind-turbine rotor aerodynamics. *Computational Mechanics*, 48:647–657, 2011.
43. K. Takizawa, T. E. Tezduyar, S. McIntyre, N. Kostov, R. Kolesar, and C. Habluetzel. Space-time VMS computation of wind-turbine rotor and tower aerodynamics. *Computational Mechanics*, 53:1–15, 2014.
  44. K. Takizawa. Computational engineering analysis with the new-generation space-time methods. *Computational Mechanics*, 54:193–211, 2014.
  45. K. Takizawa, B. Henicke, A. Puntel, T. Spielman, and T. E. Tezduyar. Space-time computational techniques for the aerodynamics of flapping wings. *Journal of Applied Mechanics*, 79:010903, 2012.
  46. K. Takizawa, B. Henicke, A. Puntel, N. Kostov, and T. E. Tezduyar. Space-time techniques for computational aerodynamics modeling of flapping wings of an actual locust. *Computational Mechanics*, 50:743–760, 2012.
  47. K. Takizawa, N. Kostov, A. Puntel, B. Henicke, and T. E. Tezduyar. Space-time computational analysis of bio-inspired flapping-wing aerodynamics of a micro aerial vehicle. *Computational Mechanics*, 50:761–778, 2012.
  48. K. Takizawa, B. Henicke, A. Puntel, N. Kostov, and T. E. Tezduyar. Computer modeling techniques for flapping-wing aerodynamics of a locust. *Computers & Fluids*, 85:125–134, 2013.
  49. K. Takizawa, T. E. Tezduyar, and N. Kostov. Sequentially-coupled space-time FSI analysis of bio-inspired flapping-wing aerodynamics of an MAV. *Computational Mechanics*, 54:213–233, 2014.
  50. K. Takizawa, T. E. Tezduyar, A. Buscher, and S. Asada. Space-time interface-tracking with topology change (ST-TC). *Computational Mechanics*, 54:955–971, 2014.
  51. K. Takizawa, T. E. Tezduyar, and A. Buscher. Space-time computational analysis of MAV flapping-wing aerodynamics with wing clapping. *Computational Mechanics*, published online, DOI: 10.1007/s00466-014-1095-0, January 2015.
  52. K. Takizawa, K. Schjodt, A. Puntel, N. Kostov, and T. E. Tezduyar. Patient-specific computer modeling of blood flow in cerebral arteries with aneurysm and stent. *Computational Mechanics*, 50:675–686, 2012.
  53. K. Takizawa, K. Schjodt, A. Puntel, N. Kostov, and T. E. Tezduyar. Patient-specific computational analysis of the influence of a stent on the unsteady flow in cerebral aneurysms. *Computational Mechanics*, 51:1061–1073, 2013.
  54. K. Takizawa, T. E. Tezduyar, A. Buscher, and S. Asada. Space-time fluid mechanics computation of heart valve models. *Computational Mechanics*, 54:973–986, 2014.
  55. H. Suito, K. Takizawa, V. Q. H. Huynh, D. Sze, and T. Ueda. FSI analysis of the blood flow and geometrical characteristics in the thoracic aorta. *Computational Mechanics*, 54:1035–1045, 2014.
  56. K. Takizawa, D. Montes, S. McIntyre, and T. E. Tezduyar. Space-time VMS methods for modeling of incompressible flows at high Reynolds numbers. *Mathematical Models and Methods in Applied Sciences*, 23:223–248, 2013.
  57. K. Takizawa, T. E. Tezduyar, and T. Kuraishi. Multiscale ST methods for thermo-fluid analysis of a ground vehicle and its tires. *Mathematical Models and Methods in Applied Sciences*, to appear, 2015.
  58. Y. Bazilevs, K. Takizawa, and T. E. Tezduyar. Challenges and directions in computational fluid-structure interaction. *Mathematical Models and Methods in Applied Sciences*, 23:215–221, 2013.
  59. K. Takizawa, D. Montes, M. Fritze, S. McIntyre, J. Boben, and T. E. Tezduyar. Methods for FSI modeling of spacecraft parachute dynamics and cover separation. *Mathematical Models and Methods in Applied Sciences*, 23:307–338, 2013.
  60. K. Takizawa, T. E. Tezduyar, J. Boben, N. Kostov, C. Boswell, and A. Buscher. Fluid-structure

26 Y. Bazilevs, A. Korobenko, J. Yan, A. Pal, S.M.I. Gohari, and S. Sarkar

- interaction modeling of clusters of spacecraft parachutes with modified geometric porosity. *Computational Mechanics*, 52:1351–1364, 2013.
61. K. Takizawa, T. E. Tezduyar, C. Boswell, R. Kolesar, and K. Montel. FSI modeling of the reefed stages and disreefing of the Orion spacecraft parachutes. *Computational Mechanics*, 54:1203–1220, 2014.
  62. K. Takizawa, T. E. Tezduyar, R. Kolesar, C. Boswell, T. Kanai, and K. Montel. Multiscale methods for gore curvature calculations from FSI modeling of spacecraft parachutes. *Computational Mechanics*, 54:1461–1476, 2014.
  63. K. Takizawa, T. E. Tezduyar, C. Boswell, Y. Tsutsui, and K. Montel. Special methods for aerodynamic-moment calculations from parachute FSI modeling. *Computational Mechanics*, published online, DOI: 10.1007/s00466-014-1074-5, October 2014.
  64. K. Takizawa, T. E. Tezduyar, and R. Kolesar. FSI modeling of the Orion spacecraft drogue parachutes. *Computational Mechanics*, published online, DOI: 10.1007/s00466-014-1108-z, December 2014.
  65. P. Kundu and I. Cohen. *Fluid Mechanics, 2nd Edition*. Elsevier, 2002.
  66. B. Sutherland. *Internal Wave Propagation*, pages 372–422. Modern Applied Mathematics. Narosa Press, New Delhi, 2005.
  67. T. J. R. Hughes. Multiscale phenomena: Green’s functions, the Dirichlet-to-Neumann formulation, subgrid scale models, bubbles, and the origins of stabilized methods. *Computer Methods in Applied Mechanics and Engineering*, 127:387–401, 1995.
  68. T. J. R. Hughes, G. Scovazzi, and L. P. Franca. Multiscale and stabilized methods. In E. Stein, R. de Borst, and T. J. R. Hughes, editors, *Encyclopedia of Computational Mechanics, Vol. 3, Fluids*, chapter 2. Wiley, 2004.
  69. A. N. Brooks and T. J. R. Hughes. Streamline upwind/Petrov-Galerkin formulations for convection dominated flows with particular emphasis on the incompressible Navier-Stokes equations. *Computer Methods in Applied Mechanics and Engineering*, 32:199–259, 1982.
  70. T. J. R. Hughes and T. E. Tezduyar. Finite element methods for first-order hyperbolic systems with particular emphasis on the compressible Euler equations. *Computer Methods in Applied Mechanics and Engineering*, 45:217–284, 1984.
  71. T. E. Tezduyar and Y. J. Park. Discontinuity capturing finite element formulations for nonlinear convection-diffusion-reaction equations. *Computer Methods in Applied Mechanics and Engineering*, 59:307–325, 1986.
  72. T. J. R. Hughes, L. P. Franca, and M. Balestra. A new finite element formulation for computational fluid dynamics: V. Circumventing the Babuška–Brezzi condition: A stable Petrov–Galerkin formulation of the Stokes problem accommodating equal-order interpolations. *Computer Methods in Applied Mechanics and Engineering*, 59:85–99, 1986.
  73. T. E. Tezduyar and Y. Osawa. Finite element stabilization parameters computed from element matrices and vectors. *Computer Methods in Applied Mechanics and Engineering*, 190:411–430, 2000.
  74. M.-C. Hsu, Y. Bazilevs, V. M. Calo, T. E. Tezduyar, and T. J. R. Hughes. Improving stability of stabilized and multiscale formulations in flow simulations at small time steps. *Computer Methods in Applied Mechanics and Engineering*, 199:828–840, 2010.
  75. M.-C. Hsu, I. Akkerman, and Y. Bazilevs. Wind turbine aerodynamics using ALE–VMS: Validation and the role of weakly enforced boundary conditions. *Computational Mechanics*, 50:499–511, 2012. doi:10.1007/s00466-012-0686-x.
  76. C. Johnson. *Numerical solution of partial differential equations by the finite element method*. Cambridge University Press, Sweden, 1987.
  77. S. C. Brenner and L. R. Scott. *The Mathematical Theory of Finite Element Methods, 2nd ed.* Springer, 2002.
  78. A. Ern and J. L. Guermond. *Theory and Practice of Finite Elements*. Springer, 2004.

79. F. Shakib, T. J. R. Hughes, and Z. Johan. A multi-element group preconditioned GMRES algorithm for nonsymmetric systems arising in finite element analysis. *Computer Methods in Applied Mechanics and Engineering*, 75:415–456, 1989.
80. T. J. R. Hughes and M. Mallet. A new finite element formulation for computational fluid dynamics: III. The generalized streamline operator for multidimensional advective-diffusive systems. *Computer Methods in Applied Mechanics and Engineering*, 58:305–328, 1986.
81. T. J. R. Hughes, G. Scovazzi, and T. E. Tezduyar. Stabilized methods for compressible flows. *Journal of Scientific Computing*, 43:343–368, 2010. DOI: 10.1007/s10915-008-9233-5.
82. D. E. Mowbray and B. S. H. Rarity. A theoretical and experimental investigation of the phase configuration of internal waves of small amplitude in a density stratified liquid. *J. Fluid Mech.*, 28:1–16, 1967.
83. B. R. Sutherland, S. B. Dalziel, G. O. Hughes, and P. F. Linden. Visualization and measurement of internal waves by “synthetic schlieren”. part 1: Vertically oscillating cylinder. *J. Fluid Mech.*, 390:93–126, 1999. doi:10.1017/S0022112099005017.
84. B. Gayen, S. Sarkar, and J. R. Taylor. Large eddy simulation of a stratified boundary layer under an oscillatory current. *J. Fluid Mech.*, 643:233–266, 2010.
85. B. Gayen and S. Sarkar. Direct and large-eddy simulations of internal tide generation at a near-critical slope. *J. Fluid Mech.*, 681:48–79, 2011.
86. Y. Bazilevs, M.-C. Hsu, and M.A. Scott. Isogeometric fluid–structure interaction analysis with emphasis on non-matching discretizations, and with application to wind turbines. *Computer Methods in Applied Mechanics and Engineering*, 249-252:28–41, 2012.
87. K. Takizawa and T. E. Tezduyar. Space–time computation techniques with continuous representation in time (ST-C). *Computational Mechanics*, 53:91–99, 2014.
88. J. Jonkman, S. Butterfield, W. Musial, and G. Scott. Definition of a 5-MW reference wind turbine for offshore system development. Technical Report NREL/TP-500-38060, National Renewable Energy Laboratory, 2009.
89. T. J. R. Hughes, J. A. Cottrell, and Y. Bazilevs. Isogeometric analysis: CAD, finite elements, NURBS, exact geometry, and mesh refinement. *Computer Methods in Applied Mechanics and Engineering*, 194:4135–4195, 2005.
90. J. A. Cottrell, T. J. R. Hughes, and Y. Bazilevs. *Isogeometric Analysis: Toward Integration of CAD and FEA*. Wiley, Chichester, 2009.